crystals

MDPI

Article

Spin-Phonon Coupling in A_2BMnO_6 (A = La, Pr, Nd, Sm, Gd; B = Co, Ni) Double-Perovskite Thin Films: Impact of the A-Site Cation Radius

Christoph Meyer [1], Philipp Ksoll [1], Vladimir Roddatis [2,3] and Vasily Moshnyaga [1,*]

[1] Erstes Physikalisches Institut, Georg-August-Universität Göttingen, Friedrich-Hund-Platz 1, 37077 Göttingen, Germany; christoph.meyer@phys.uni-goettingen.de (C.M.); philipp.ksoll@stud.uni-goettingen.de (P.K.)
[2] Institut für Materialphysik, Georg-August-Universität Göttingen, Friedrich-Hund-Platz 1, 37077 Göttingen, Germany; vladimir.roddatis@gfz-potsdam.de
[3] GFZ German Research Centre for Geosciences, Helmholtz Centre Potsdam, Telegrafenberg, 14473 Potsdam, Germany
* Correspondence: vmosnea@gwdg.de

Abstract: Two series of B-site ordered, double-perovskite A_2CoMnO_6 and A_2NiMnO_6 (A = La, Pr, Nd, Sm, Gd) epitaxial films with thickness d ~ 100 nm were grown on $SrTiO_3$(111) substrates via metalorganic aerosol deposition. Polarization and temperature-dependent Raman spectroscopy were carried out in order to determine the spin-phonon coupling constant, λ, and the impact of the A-site cation radius on the phonon properties. The reduction of the A-site cation radius from La^{3+} down to Gd^{3+} systematically shifts the Raman modes to lower wavenumbers, and decreases the magnetization-induced softening of the Ag breathing mode, described by the spin-phonon coupling constant, λ, which changes from λ = 1.42 cm^{-1} (La_2CoMnO_6) and λ = 1.53 cm^{-1} (La_2NiMnO_6) down to λ = 0.58 cm^{-1} (Gd_2CoMnO_6) and λ = 0.44 cm^{-1} (Gd_2NiMnO_6). A similar effect of the A-cation radius was established for the c-lattice parameter and Curie temperature, TC, in this series of double-perovskite films. Our observations directly demonstrate a strong impact of the lattice structure on the ferromagnetic superexchange interaction in double perovskites. Moreover, the A_2CoMnO_6 and A_2NiMnO_6 series exhibit very similar behavior of spin-phonon coupling due to the only moderate difference of Co^{2+} and Ni^{2+} cation size.

Keywords: double perovskites; thin films; Raman spectroscopy; spin-phonon coupling

Citation: Meyer, C.; Ksoll, P.; Roddatis, V.; Moshnyaga, V. Spin-Phonon Coupling in A_2BMnO_6 (A = La, Pr, Nd, Sm, Gd; B = Co, Ni) Double-Perovskite Thin Films: Impact of the A-Site Cation Radius. *Crystals* **2021**, *11*, 747. https://doi.org/10.3390/cryst11070747

Academic Editors: Charles Rosenblatt, Helmut Cölfen, Abel Moreno, Sławomir Grabowski and Shujun Zhang

Received: 18 May 2021
Accepted: 23 June 2021
Published: 26 June 2021

1. Introduction

Double perovskites of the family A_2BMnO_6 (A = rare earth, B = Co, Ni), with a monoclinic $P12_1/n1$ structure, are promising materials for spintronic applications due to the presence of ferromagnetic ordering, magnetodielectric coupling, and multiferroic behavior [1–7]. Furthermore, they represent an attractive model system, in which the fundamental coupling between spin, charge, and lattice degrees of freedom—and, thus, their electromagnetic properties—strongly depend on the A-site cation radius [5–7], on the oxidation state of B-site cations [2,8,9] and, finally, on the degree of the B-site ordering [8–13].

In this context, Raman spectroscopy as a nondestructive tool represents a powerful way to distinguish between the monoclinic $P12_1/n1$ B-site ordered and the orthorhombic Pbnm B-site disordered A_2BMnO_6 variants; this is possible due to the different symmetry and selection rules of the corresponding Raman modes [1,14]. As a consequence, polarized Raman spectroscopy has been extensively applied to A_2BMnO_6 double-perovskite bulk samples [6,15–17] and thin films [1,10,14,15,18–22]. In addition, the spin-phonon coupling [1,10,14,16,17,19–21] and structural changes [10,15,22] of the double perovskites can be directly elucidated from the temperature development of the Raman spectra.

Here, we report the impact of the A-site cation size on the structural, magnetic, and phonon properties of A_2CoMnO_6 and A_2NiMnO_6 (A = La, Pr, Nd, Sm, Gd) epitaxial films grown on (111)-oriented $SrTiO_3$ (STO) substrates via a metalorganic aerosol deposition (MAD) technique [23]. The easy stoichiometry control within MAD is very useful for the growth of high-quality epitaxial films with different compositions. Polarization and temperature-dependent Raman spectroscopy carried out for temperatures T = 80–300 K allow us to relate the characteristic changes in the Raman spectra, induced by the A-cation size, to the changes in structure and magnetism. We observed the systematic reduction of the spin-phonon coupling by decreasing the A-site cation radius, and discussed it in the framework of variation of the internal chemical pressure induced by A-site cations.

2. Experimental Details

Double-perovskite A_2CoMnO_6 and A_2NiMnO_6 (A = La, Pr, Nd, Sm, Gd; B = Co, Ni)—further referred to as Co- and Ni-series, respectively—epitaxial thin films with thickness d ~ 100 nm were grown on $SrTiO_3$ (STO) substrates with (111) orientation by means of MAD [23], using a solution of acetylacetonates for the A- and B-site cations in dimethylformamide (DMF) under ambient oxygen partial pressure (pO_2 ~ 0.2 bar), with growth rates of r ~ 6 nm/min, substrate temperature of T_{sub} ~ 900–950 °C, and a heating/cooling rate of ~50 K/min before and after deposition [10,11,24]. X-ray reflection (XRR) and X-ray diffraction (XRD, Cu-K_α radiation, Bruker AXS D8 Advance) were used to determine the thickness, the quality, and the out-of-plane lattice parameters of the films. Temperature-dependent magnetization was measured using a SQUID magnetometer (MPMS 3, Quantum Design) at temperatures of T = 5–400 K and under an external magnetic field of H = 1000 Oe. Raman spectra were recorded using a LabRAM HR Evolution (HORIBA Jobin Yvon) spectrometer in the backscattered top-illumination geometry. A Linkam THMS350EV thermal vacuum stage, cooled by liquid nitrogen, was used for temperature-dependent measurements in the temperature range T = 80–400 K. The sample illumination and the collection of backscattered light was conducted using a 50× magnification long working distance objective (Olympus, NA = 0.5). The excitation was carried out using a linear polarized Nd:YAG laser (λ = 532 nm, Laser Quantum torus 532, second harmonic generation) with an effective incident power of P ~ 2 mW at the film surface and a laser spot size of ~1 μm^2 laterally. Polarized Raman spectra were recorded in a sample reference system with $X \| [11\bar{2}]$ parallel to the incident laser polarization, $Y \| [\bar{1}10]$ perpendicular to it, and $Z \| [111]$ in the direction of light propagation. The scattered light polarization was filtered by an analyzer with two configurations (x and y) in front of the detector. Consequently, XX implies parallel scattering with the analyzer aligned parallel to the incident laser polarization, while XY is a cross-scattering polarization configuration with the analyzer aligned perpendicular to it. Transmission electron microscopy was performed using a FEI Titan 80–300 G2 environmental transmission electron microscope (TEM) operated at an acceleration voltage of 300 kV.

3. Results

To characterize the impact of the A-site cation size on the structure, we performed the XRD measurements on all of the grown films (see Supplementary Materials (SM), Figure S1 for details). XRD and TEM (SM, Figure S2) evidence an epitaxial growth for both series of samples, in good agreement with previously reported MAD-grown, double-perovskite films [10,11,18]. In Figure 1a we present the evaluated pseudocubic out-of-plane lattice parameters $c_{pc} = c(111)/\sqrt{3}$ of the Co- and Ni-series on STO(111) as a function of the A-site cation radius, taken from Ref. [25] for coordination number CN = 8. One can see that c_{pc} systematically deceases with the decrease in the A-site cation radius, and the data for both film series can be quite well described by linear fits. Note that the A_2CoMnO_6 series shows slightly larger lattice parameters than the A_2NiMnO_6 series, which can be attributed to the slightly larger B-site cation radius of Co^{2+} compared to the Ni^{2+} cation—i.e., 74.5 pm for high-spin (HS)-Co^{2+} vs. 69 pm for Ni^{2+}; CN = 6, Ref. [26]. Related to the corresponding

polycrystalline bulk samples of both double-perovskite series [5–7], the pseudocubic out-of-plane lattice parameters are slightly decreased due to an in-plane tensile epitaxy strain from the STO substrate, having a larger in-plane lattice parameter a_{STO} = 0.3905 nm [25], and resulting in a lattice compression in the out-of-plane direction. As the lattice parameter shrinks further by reducing the A-site cation size, the out-of-plane compressive strain $\varepsilon = (c_{pc} - a_{sub})/a_{sub}$ of the films systematically increases from $\varepsilon = -0.77\%$ for La_2CoMnO_6 (LCMO) and $\varepsilon = -0.87\%$ for La_2NiMnO_6 (LNMO) to $\varepsilon = -3.76\%$ for Gd_2CoMnO_6 (GCMO) and $\varepsilon = -3.99\%$ for Gd_2NiMnO_6 (GNMO).

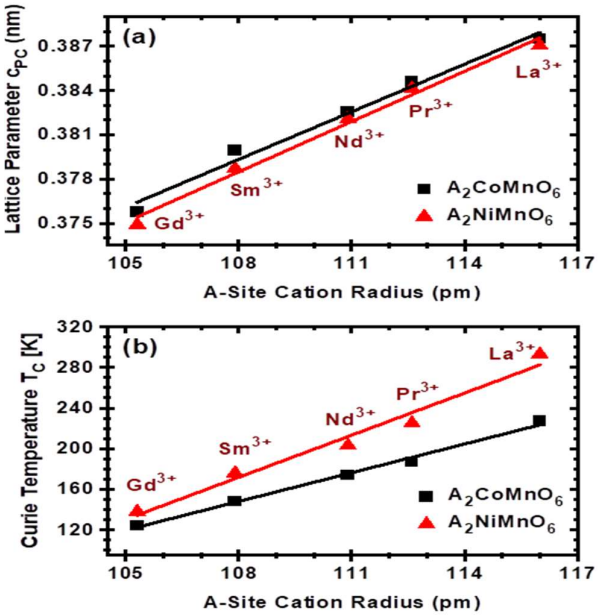

Figure 1. The pseudocubic out-of-plane lattice parameters, c_{pc}, (**a**) and the Curie temperatures, T_C, for the paramagnetic-to-ferromagnetic phase transition (**b**) of the B-site-ordered A_2CoMnO_6 and A_2NiMNO_6 double-perovskite thin film series on STO(111) as a function of the A-site rare earth cation radius. Both developments exhibit an almost linear behavior in this context.

In Figure 1b, the values of Curie temperatures, T_C, for the Co- and Ni-series as a function of the A-site cation radius are presented; the corresponding magnetization M(T) curves are shown in Figures S3 and S4 in SM. T_C values were calculated from the minimum of the temperature coefficient of magnetization, TCM = (1/M) (dM/dT). In addition, a systematic and almost linear reduction (solid lines for the linear approximation) of T_C was observed here by decreasing the A-site cation size from Gd^{3+} to Gd^{3+}. A similar decrease of T_C with decreasing r_A was obtained in recent studies on polycrystalline A_2CoMnO_6 and A_2NiMnO_6 bulk samples [5–7], and was assigned to the successive reduction of the Co^{2+}-O^{2-}-Mn^{4+} and the Ni^{2+}-O^{2-}-Mn^{4+} bond angles; this reduces the overlap of Mn(e_g) and O(2p) orbitals, and causes the apparent reduction of the ferromagnetic superexchange interaction between the two B-site cation species [5–7]. The higher Curie temperatures, T_C, for the A_2NiMnO_6 series compared to the A_2CoMnO_6 films with the same A-site cation also indicate a stronger orbital overlap of the bonds between the (Ni/Mn)O_6 octahedra compared to those of the (Co/Mn)O_6 octahedra [6], although the differences in T_C decrease by reducing the A-site cation size; this also displays the strong impact of the cations and the internal chemical pressure on the magnetic properties of the A_2BMnO_6 double-perovskite system. In addition to the optimally high values of T_C in films of both Co and Ni series, the saturation magnetization measured at T = 5 K was found to be close to the theoretical values of 6 μ_B/f.u and 5 μ_B/f.u for the Co- and Mn-series, respectively. All of this indicates a high degree of B-site ordering in studied samples.

The Raman spectra recorded at T = 300 K of the Co- and Ni-series of double-perovskite thin films are shown in Figure 2a,b, respectively, in the parallel XX-scattering configuration,

whereas Figure 2c,d show the corresponding Raman spectra in the crossed XY-scattering configuration. All films exhibit very similar Raman spectra, with two significant features: first, a strong and sharp mode at a Raman shift of ~630–675 cm^{-1}, and second, a broader and less intensive band at around ~470–530 cm^{-1}. Theoretical lattice dynamical calculations (LDCs) for LCMO [14] assigned the sharp mode to a symmetric stretching of the $(Co/Mn)O_6$ and $(Ni/Mn)O_6$ octahedra (breathing mode), whereas the broader band relates to a mixed type of antisymmetric stretching and bending of the octahedra (mixed mode). For B-site-ordered double perovskites of A_2CoMnO_6 and A_2NiMnO_6 with a monoclinic $P12_1/n1$ structure, the breathing mode is predicted to have A_g symmetry, which is allowed in the parallel XX-scattering and is forbidden in the crossed XY-scattering configurations; the mixed mode shows a B_g symmetry with the opposite Raman selection rules [14,15,18,20]. From the polarized Raman spectra in Figure 2a–d, it is evident that all films follow this prediction for the monoclinic $P12_1/n1$ structure. The additional observed modes around ~1200–1350 cm^{-1} represent second-order overtones of the breathing mode and a breathing/mixed mode combination [18], confirming the high crystalline quality of the grown films.

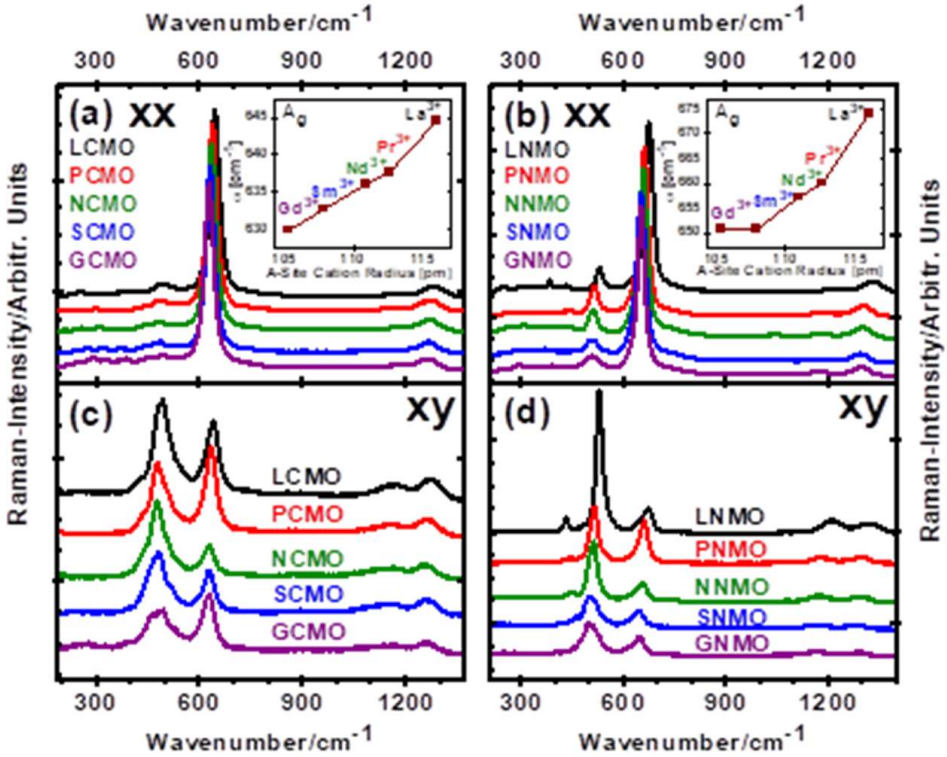

Figure 2. Polarized Raman spectra (at T = 300 K) of the two double-perovskite A_2CoMnO_6 (**a**,**c**) and A_2NiMnO_6 (**b**,**d**) thin film series on STO(111) in the parallel XX-scattering configuration (**a**,**b**) and in the crossed XY-scattering configuration (**c**,**d**). The insets in (**a**,**b**) show the development of the position of the Ag breathing modes of the A_2CoMnO_6 and A_2NiMnO_6 film series in the Raman spectra with XX-scattering configuration as a function of the A-site rare earth cation size.

Furthermore, a clear impact of the A- and B-site cations on the Raman spectra can be seen. Namely, the position of all Raman modes of the A_2NiMnO_6 series is shifted by ~20–30 cm^{-1} to higher wavenumbers compared to those in the corresponding A_2CoMnO_6 series, due to the larger degree of covalence of the A–O and Ni/Mn–O bonds in the A_2NiMnO_6 system [6]. Moreover, the radius of the A-site cation has a significant impact on the position of the Raman modes as well. For both film series, a systematic softening of all Raman modes when decreasing the A-site cation radius was observed, indicating an increase in the Co(Ni)/Mn–O bond length [9,27]. For the A_g breathing mode in the

parallel XX-scattering spectra, the development for both series is illustrated in the insets of Figure 2a,b. A similarity of the phonon behavior with that of the c-lattice parameter (see Figure 1a) and T_C (Figure 1b) as a function of the A-site cation radius evidences a strong interconnection of the structural, magnetic, and lattice properties.

In Figure 3a,b the temperature dependences of the Raman shift $\omega(T)$ of the A_g mode in the Raman spectra for the Co- and Ni-series, with different A-site cations—A = La, Pr, Nd, Sm, and Gd—are shown. In general, the temperature dependences of the positions of the Raman modes result from the anharmonic contribution to the potential energy of the atomic vibrations. By considering cubic anharmonic constants on the potential energy, the scattering can be characterized by a three-phonon process, such that the Raman mode position as a function of the temperature can be described as [28,29]:

$$\omega_{\text{anh.}}(T) = \omega_0 + C\left(1 + \frac{2}{\exp(\hbar\omega_0/2k_BT) - 1}\right) \quad (1)$$

where ω_0 is the position of a Raman mode at T = 0 K, and C is an anharmonic constant, both of which were taken as adjustable parameters to fit the temperature dependence of the experimentally determined position of the A_g mode. One can see in Figure 3a,b that the anharmonic model (red curves) of the A_g mode position $\omega(T)$ fits the experimental data (black data points) for temperatures $T \geq T_C$ within the paramagnetic phase of the double-perovskite thin films nicely. However, for all films of the Co- and Ni-series, a distinct deviation from the anharmonic model approximation occurs for 80 K < T < T_C—namely, one can see a significant softening of the A_g breathing mode, initiated by the transition into a ferromagnetic phase at T_C and continuously increased by a subsequent cooling to lower temperatures. Comparing the position of the A_g mode at the lowest temperature T = 80 K with that given by anharmonic approximation for different films, it is evident that the extent of the softening appears to be coupled to the radius of the A-site cations—i.e., the largest A-site cation Gd^{3+} results in the strongest softening, which then decreases systematically by reducing the A-site radius to Gd^{3+}. This is very similar to the above-shown effects of the A-site cation radius on the c-lattice parameter (Figure 1a), on the T_C (Figure 1b), and on the softening of the breathing mode with decreasing r_A, as shown in Figure 2a,b. Taken together, these data offer a clear indication of the connection between the mode softening, the lattice structure, and the magnetic properties.

The softening of the A_g breathing mode at $T < T_C$ originates from a phonon renormalization induced by ferromagnetic ordering, also observed for ferromagnetic manganites [29,30] and cobaltates [31], resulting in a coupling between magnetism and lattice known as a spin-phonon coupling. Considering the nearest-neighbor interaction, the phonon renormalization $\Delta\omega(T) = \omega(T) - \omega_{\text{anh.}}(T)$ is proportional to the spin–spin correlation function $\langle S_i \cdot S_j \rangle$ of the spins at the ith and jth sites, which is proportional in a molecular mean-field approximation to the normalized average magnetization $M^2(T)/M^2_{max}$ per magnetic ion at temperature T [14,29–31]. As there are four nearest B′-site cation neighbors for each B-site cation in the $A_2BB'O_6$ double perovskites with a rock-salt-type B-site ordering, the phonon renormalization $\Delta\omega(T)$ can be written as [30–32]:

$$\Delta\omega(T) = \omega(T) - \omega_{\text{anh.}}(T) \approx -\lambda S_i \cdot S_j \approx -4\lambda \frac{M^2(T)}{M^2_{\text{max}}} \quad (2)$$

Within this model, the spin-phonon coupling is quantified by the spin-phonon coupling constant, λ, whereas M_{max} is the saturation magnetization at T = 0 K. In Figures 4a–e and 5a–e we present the softening $\Delta\omega(T) = \omega(T) - \omega_{\text{anh.}}(T)$ of the A_g breathing mode plotted against squared normalized magnetization $M^2(T)/M^2_{max}$ for the Co- and Ni-film series, respectively. An excellent agreement between the $\Delta\omega(T)$ and magnetization data for all films at temperatures of $T < T_C$ verifies that the A_g mode softening arises from the spin-phonon coupling. It is evident that the softening, starting at

T_C, increases with increasing magnetization in the film by cooling; hence, a significant spin-phonon coupling is present for all of our films in their ferromagnetic phases.

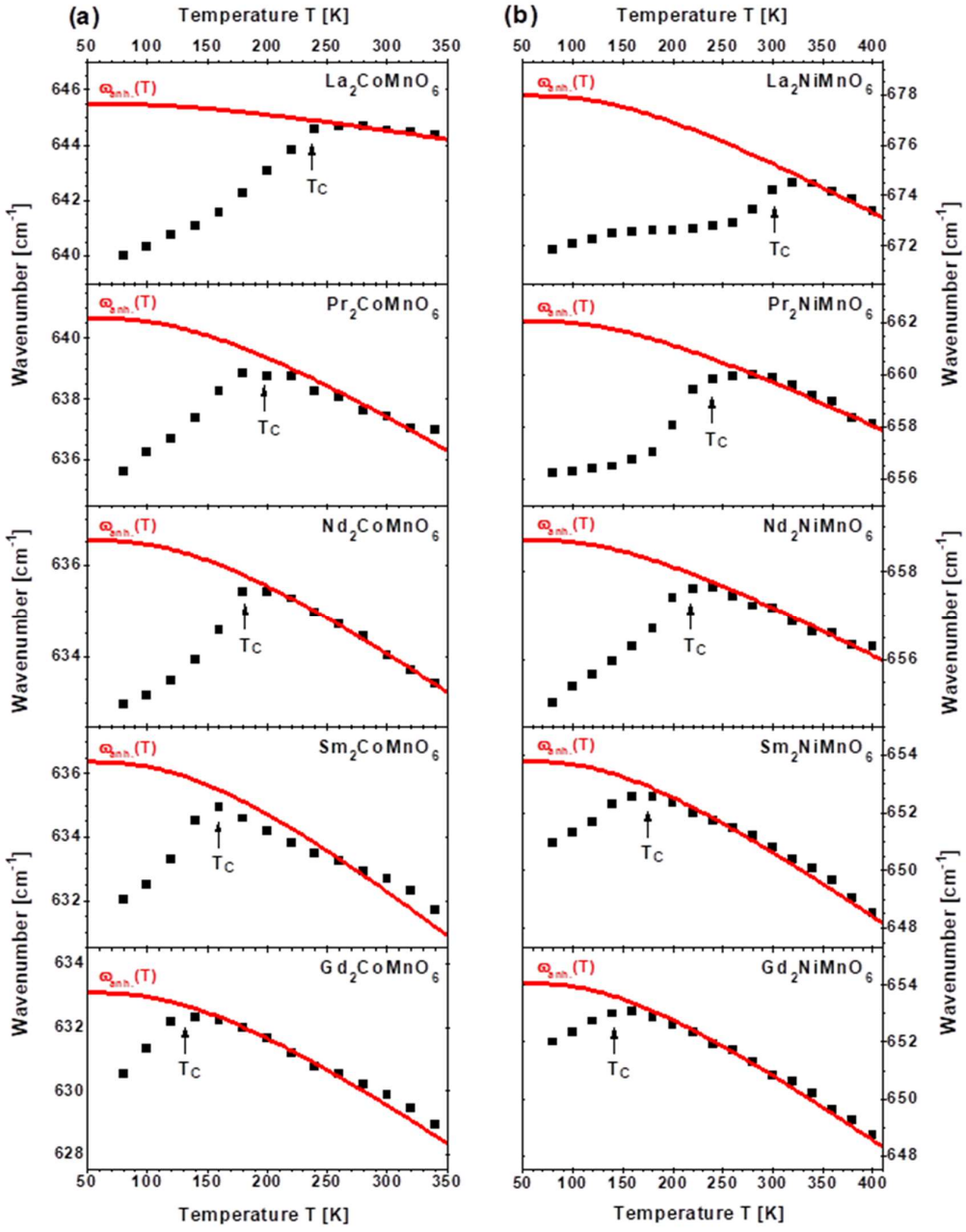

Figure 3. Temperature dependence of the A_g breathing mode position in the A_2CoMnO_6 (**a**) and the A_2NiMnO_6 (**b**) thin film series (thickness d ~ 100 nm) with A = La, Pr, Nd, Sm, and Gd on STO(111) in the Raman spectra (unpolarized). The red solid lines denote the approximation from the anharmonic three-phonon model, which fits nicely for $T > T_C$ in the paramagnetic phase of the films.

The shift $\Delta\omega(T)$ of the A_g breathing mode, plotted against the magnetization $M^2(T)/M^2_{max}$, can be described by a linear approximation—as shown for both film series in Figures 4f and 5f—and the spin-phonon coupling strength is determined by the corresponding slope S = 4λ. [10,16,19,31] One can see a systematic decrease in the slope and, hence, in the spin-phonon coupling constant when the A-site cation radius is reduced from the largest cation Gd^{3+} to the smallest cation Gd^{3+} within the A_2CoMnO_6 and A_2NiMnO_6 film series. The corresponding values for the spin-phonon coupling strength, λ, are presented for both series as a function of the A-site cation radius [26] in Figure 6.

For the A_2CoMnO_6 film series, the maximal value of $\lambda = 1.42$ cm^{-1}, obtained for LCMO, reduces systematically with the decreasing size of the A-cation, down to $\lambda = 0.58$ cm^{-1} (GCMO). For the A_2NiMnO_6 films, the maximal value of $\lambda = 1.53$ cm^{-1} (LNMO) reduces to $\lambda = 0.44$ cm^{-1} (GNMO). Note that the λ values for GCMO and GNMO are likely underestimated, since these films show an enhanced saturation magnetization (see Table S1 in the SM) due to the strong contribution of the magnetic moment of Gd. Hence, a systematic and similar decrease in the spin-phonon coupling strength, λ, by reducing the A-site cation radius is observed for both series. A similar behavior was observed recently for $A_2CoMnO_6/LaAlO_3(001)$ films (A = Pr, Nd, Sm) [19] and polycrystalline bulk samples (A = La, Pr, Nd) [16]. Remarkably, very different λ-values were determined in thin films and bulk samples: a PCMO film and a bulk sample show $\lambda = 1.61$ cm^{-1} and $\lambda = 0.51$ cm^{-1}, respectively. As for the A_2NiMnO_6 series, no influence of the A-site cation radius on the spin-phonon coupling was detected in bulk samples for A = La, Pr, Nd, Gd, Y [17], in contradiction to our results for A_2NiMnO_6/STO(111) films (see Figure 6).

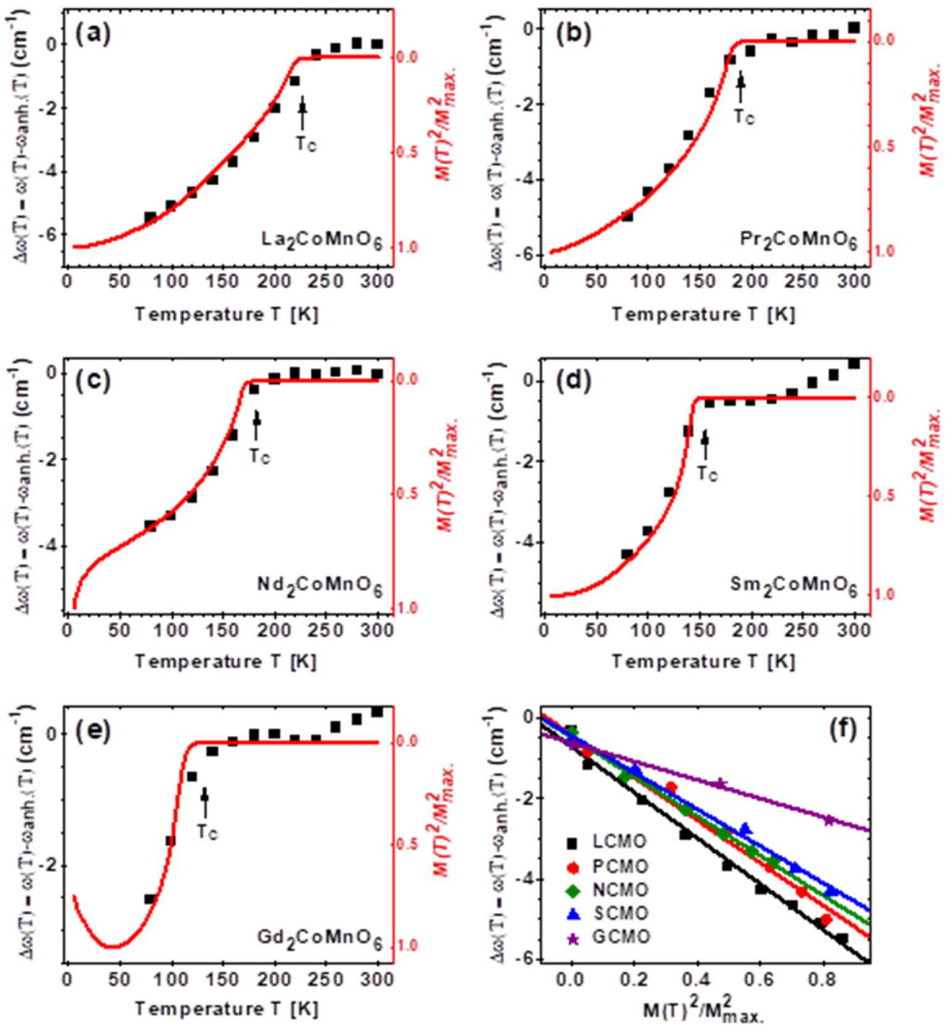

Figure 4. The development of the deviation $\Delta\omega(T)$ of the A_g breathing mode position from the anharmonic approximation (phonon renormalization; black data points) and the squared magnetization $M^2\ (T)/M^2_{max}$ with the temperature T for the LCMO (**a**), PCMO (**b**), NCMO (**c**), SCMO (**d**), and GCMO (**e**) double-perovskite thin films on STO(111). Additionally, in (**f**), the corresponding linear approximation between the phonon renormalization $\Delta\omega(T)$ and the magnetization $M^2\ (T)/M^2_{max}$ is presented for each of the different A_2CoMnO_6/STO(111) thin films of the series.

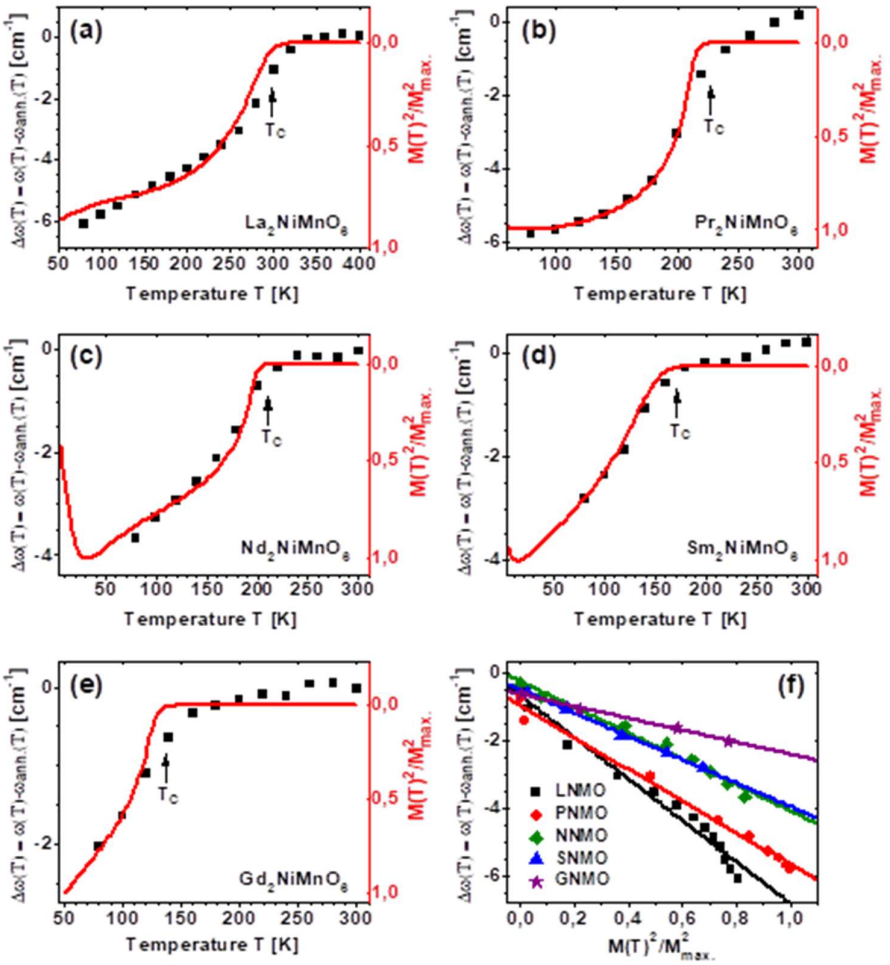

Figure 5. The development of the deviation $\Delta\omega$(T) of the A_g breathing mode position from the anharmonic approximation (phonon renormalization; black data points) and the squared magnetization $M^2(T)/M^2_{max.}$ with the temperature T for the LNMO (**a**), PNMO (**b**), NNMO (**c**), SNMO (**d**), and GNMO (**e**) double-perovskite thin films on STO(111). Additionally, in (**f**), the corresponding linear approximation between the phonon renormalization $\Delta\omega$(T) and the magnetization M^2 *(T)*/$M^2{}_{max}$ is presented for each of the different A_2NiMnO_6/STO(111) thin films of the series.

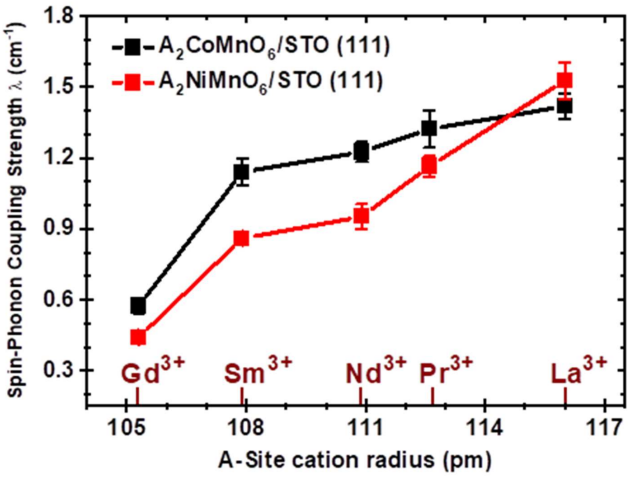

Figure 6. The spin-phonon coupling strength, λ, of the B-site-ordered A_2CoMnO_6 and A_2NiMNO_6 thin film series on STO(111) as a function of the A-site cation radius. The values were extracted from the phonon renormalization of the A_g breathing mode in the ferromagnetic phase below T_C.

4. Discussion

To elucidate the origin of the A-site cation influence on the spin-phonon coupling in double-perovskite films, the intrinsic and extrinsic mechanisms should be considered. In general, the systematic decrease in the spin-phonon coupling strength, λ, for smaller A-site cations reflects the impact of chemical pressure on the structure–property (magnetic and phononic) relationship. Initially, the orbital overlap and the apparent ferromagnetic superexchange depend on the Co^{2+}–O^{2-}–Mn^{4+} or Ni^{2+}–O^{2-}–Mn^{4+} bond angles between the B-site cations [5–7]. This is shown in Figure 1b for the A_2CoMnO_6 and the A_2NiMnO_6 series, for which a reduction in the A-site cation size from Gd^{3+} to Gd^{3+} leads to a systematic decrease in T_C due to the chemical-pressure-induced decrease in the bond angle. Simultaneously, the reduction of the A-site cation radius modifies the internal bond lengths, yielding a decrease in the pseudocubic c-lattice parameter [5–7,33] (Figure 1a), an increase in the lattice mismatch and, finally, an enhancement of the epitaxy stress in films grown on the STO(111) substrates. As a result, the force constants of the perovskite lattice [30,32] also increase, and the lattice gets stiffer, as evidenced by the significant shift of the A_g breathing mode in the Raman spectra towards larger wavenumbers (Figure 2a,b). As a consequence, the decrease in the A-site cation radius results in a systematic reduction of both the magnetic superexchange interaction and the spin-phonon coupling, as the latter connects magnetic and phonon properties. A similar behavior was seen also for the rare earth $RMnO_3$ manganites [30,32].

Comparing the A_2CoMnO_6 and the A_2NiMnO_6 double-perovskite film series, the spin-phonon coupling strength, λ, for the same A-site cation exhibits only small differences, indicating a weak impact of the Co^{2+} and Ni^{2+} cations on the spin-phonon coupling. In general, the A_2CoMnO_6 film series shows slightly larger λ values (the only exception being A = La) than the A_2NiMnO_6 film series, although T_C values are significantly higher for the A_2NiMnO_6 series (Figure 1b). As the cation size of Co^{2+} and Ni^{2+} is comparable (74.5 pm for HS-Co^{2+} vs. 69 pm for Ni^{2+}; CN = 6, Ref. [26]), and the lattice parameters are also similar (Figure 1a), the different spin contributions of HS–Co^{2+}/Ni^{2+}, and their impact on the bonds, force constants, and phonon properties (Figure 2a–d), must be involved. Obviously, the overall interplay results in a comparable spin-phonon coupling for both series. Recent studies on the A_2CoMnO_6 series showed similar values for the coupling strength, with $\lambda = 1.61$ cm^{-1} for PCMO, $\lambda = 1.20$ cm^{-1} for NCMO, and $\lambda = 1.16$ cm^{-1} for SCMO for films on LAO(100) substrates [19], and $\lambda \sim 1.4$–2.1 cm^{-1}, depending on the substrate, for LCMO thin films [10], whereas for polycrystalline bulk PCMO with $\lambda = 0.51$ cm^{-1}, a significantly lower coupling was obtained [16]. For the A_2NiMnO_6 series, no comparative values are available. Recent studies on polycrystalline A_2NiMnO_6 bulk samples showed no A-site cation influence, but from the A_g breathing mode softening, the coupling strength can be estimated roughly to $\lambda \sim 0.6$–0.7 cm^{-1} for the whole series [17], which is again significantly lower than for our A_2NiMnO_6 thin films.

An explanation for this discrepancy can be given by the sample characteristics; whereas the epitaxial thin films exhibit a high crystalline quality and are in-plane strained due to the lattice misfit [10,12,19,24], the strain effects are absent for the polycrystalline bulk samples, but problems concerning the oxygen stoichiometry can occur and play a crucial role [8,9,16]. Furthermore, the degree of the B-site ordering of the double-perovskites must be included for a complete discussion [10,12,20,21]. Beginning with the strain, it is argued that for the case of A_2CoMnO_6 films on LAO(100), the compressive biaxial strain has a significant influence on the magnetic interaction and the spin-phonon coupling, due to a reduction in oxygen vacancies and a higher degree of B-site ordering compared to bulk samples [16,19]. Our recent study on the B-site-ordered LCMO thin films with a (111) out-of-plane-orientation on various substrates also reveals a strong strain impact [10]. In this context, the largest spin-phonon coupling strength of $\lambda \sim 2.1$ cm^{-1} was observed for LCMO(111) films on Al_2O_3(0001) and on $(LaAlO_3)_{0.3}(Sr_2TaAlO_6)_{0.7}$(111)(LSAT) substrates, actuating a small, compressive, in-plane strain. This coupling constant is significantly

larger than $\lambda \sim 1.4$–1.5 cm^{-1} (see Ref. [10] and the present study), obtained on LCMO(111) films grown on substrates with a larger lattice mismatch, such as LAO(111) and STO(111).

On the other hand, the spin-phonon coupling of the double-perovskite A_2BMnO_6 is affected by the degree of the B-site ordering, as it directly depends on structural and magnetic properties [8–12]. For B-site-ordered LCMO and LNMO films, this is reflected by a significant increase in the softening of the A_g breathing mode in the ferromagnetic phase, and by the corresponding spin-phonon coupling for the B-site-ordered films compared to partially or fully disordered systems [10,20,21]. For LCMO thin films on c-orientated Al_2O_3(0001), this results in a spin-phonon coupling strength of $\lambda \sim 2.1$ cm^{-1} in the case of B-site ordering, and a decrease to $\lambda \sim 1.7$ cm^{-1} for a partially B-site-disordered film [10]. Additionally, the B-site ordering in the double-perovskite films can be stimulated and improved by a compressive in-plane strain, due to a different distortion of the B/B'O_6 octahedra [12]. In combination with the higher crystalline quality of the epitaxial thin films, a higher degree of B-site ordering—and, hence, a stronger mode softening and spin-phonon coupling compared to polycrystalline, double-perovskite bulk samples—is achieved. For partially B-site-disordered or polycrystalline bulk double perovskites, this also results in a decreased impact of the A-site cation on the coupling strength, as the crystal quality, ordering, and strain have a significantly stronger influence [10,16,17,19–21]. Conversely, the spin-phonon coupling strength as an indicator of the crystal quality depicts a direct way to characterize and improve the suitability of a double-perovskite material for technological applications.

5. Conclusions

Epitaxial films of the B-site-ordered A_2CoMnO_6 and A_2NiMnO_6 (A = La, Pr, Nd, Sm, Gd) double-perovskite series with a monoclinic $P12_1/n1$ structure were grown on $SrTiO_3$(111) substrates using the MAD technique, in order to determine the impact of the A-site cation size on the structural, magnetic, and phonon properties. By carrying out polarization and temperature-dependent Raman measurements, the anomalous softening of the breathing mode in the ferromagnetic phase, and its dependence on the size of A-site cations, were revealed in both film series. The results were discussed within the influence of the A-site-induced variation of internal chemical pressure on the spin–lattice interaction, quantified by the corresponding spin-phonon coupling strength, λ. We observed a systematic reduction in λ by decreasing the size of the A-cation, which is very similar to the changes in the c-lattice parameters and Curie temperatures actuated by the A-cation size. Thus, the spin-phonon coupling constant—correlating structural, magnetic, and phonon properties together—displays the strong impact of the A-site cation size in the A_2CoMnO_6 and A_2NiMnO_6 double perovskites, and depicts a promising way to improve the material suitability of various double-perovskite systems for technological applications.

Supplementary Materials: The following are available online at https://www.mdpi.com/article/10.3390/cryst11070747/s1, Figure S1: XRD spectra of the A_2CoMnO_6/STO (111) (A = La, Pr, Nd, Sm, Gd) double perovskite thin film series (thickness d ~ 100 nm) together with a STO (111) pattern around the STO (111) reflex; Figure S2: XRD spectra of the A_2NiMnO_6/STO (111) (A = La, Pr, Nd, Sm, Gd) double perovskite thin film series (thickness d~100 nm) together with a STO (111) pattern around the STO (111) reflex; Figure S3: Temperature dependent M(T) magnetization curves (FCC and ZFC, H = 1000 Oe) of the A_2CoMnO_6/STO (111) (A = La, Pr, Nd, Sm, Gd) double perovskite thin film series. Figure S4: Temperature dependent M(T) magnetization curves (FCC and ZFC, H = 10000 Oe) of the A_2NiMnO_6/STO (111) (A = La, Pr, Nd, Sm, Gd) double perovskite thin film series. Table S1: Magnetic characteristics of Co- and Ni-series films.

Author Contributions: Conceptualization, C.M. and V.M.; methodology, C.M.; software, C.M., V.R.; validation, V.M.; formal analysis, C.M.; P.K.; investigation, C.M.; resources, V.M.; V.R.; data curation, C.M.; P.K.; writing—original draft preparation, C.M.; writing—review and editing, V.M.; V.R.; supervision, V.M.; project administration, V.M.; V.R.; funding acquisition, V.R.; V.M; All authors have read and agreed to the published version of the manuscript.

Funding: This research was funded by the Deutsche Forschungsgemeinschaft (DFG) via SFB 1073 (TP B04 and A02) and projects MO-2255/4 and RO-5387/3-1.

Institutional Review Board Statement: Not applicable.

Informed Consent Statement: Not applicable.

Data Availability Statement: Not applicable.

Acknowledgments: We acknowledge the financial support from the Deutsche Forschungsgemeinschaft (DFG) via SFB 1073 (TP B04 and A02) and projects MO-2255/4 and RO-5387/3-1. V.R thanks the Collaborative Laboratory and User Facility for Electron Microscopy (CLUE) at the University of Göttingen for the use of equipment.

Conflicts of Interest: The authors declare no conflict of interest.

References

1. Padhan, P.; Gupta, A. *Functional Metal Oxides*; Ogale, S.B., Venkatesan, T.V., Blamire, M.G., Eds.; Wiley VCH Springer: Weinheim, Germany, 2013; pp. 51–88.
2. Vasala, S.; Karppinen, M. $A_2B'B''O_6$ perovskites: A review. *Prog. Solid State Chem.* **2015**, *43*, 1–36. [CrossRef]
3. Shimakawa, Y.; Azuma, M.; Ichikawa, N. Multiferroic Compounds with Double-Perovskite Structures. *Materials* **2011**, *4*, 153–168. [CrossRef]
4. Singh, M.P.; Truong, K.D.; Fournier, P. Magnetodielectric effect in double perovskite La_2CoMnO_6 thin films. *Appl. Phys. Lett.* **2007**, *91*, 042504. [CrossRef]
5. Kim, M.K.; Moon, J.Y.; Choi, H.Y.; Oh, S.H.; Lee, N.; Choi, Y.J. Investigation of the magnetic properties in double perovskite R_2CoMnO_6 single crystals (R = Rare earth: La to Lu). *J. Phys. Condens. Matter* **2015**, *27*, 426002. [CrossRef] [PubMed]
6. Bull, C.L.; McMillan, P.F. Raman scattering study and electrical properties characterization of elpasolite perovskites $Ln_2(BB')O_6$ (Ln = La, Sm ... Gd and B, B′ = Ni, Co, Mn). *J. Solid State Chem.* **2004**, *177*, 2323–2328. [CrossRef]
7. Booth, R.; Fillman, R.; Whitaker, H.; Nag, A.; Tiwari, R.; Ramanujachary, K.; Gopalakrishnan, J.; Lofland, S. An investigation of structural, magnetic and dielectric properties of R_2NiMnO_6 (R = rare earth, Y). *Mater. Res. Bull.* **2009**, *44*, 1559–1564. [CrossRef]
8. Dass, R.I.; Goodenough, J.B. Multiple magnetic phases of $La_2CoMnO_{6-\delta}$ ($0 < \sim\delta < \sim 0.05$). *Phys. Rev. B* **2003**, *67*, 014401.
9. Dass, R.I.; Yan, J.-Q.; Goodenough, J.B. Oxygen stoichiometry, ferromagnetism, and transport properties of $La_{2-x}NiMnO_{6+\delta}$. *Phys. Rev. B* **2003**, *68*, 064415. [CrossRef]
10. Meyer, C.; Roddatis, V.; Ksoll, P.; Damaschke, B.; Moshnyaga, V. Structure, magnetism, and spin-phonon coupling in heteroepitaxial La_2CoMnO_6/Al_2O_3 (0001) films. *Phys. Rev. B* **2018**, *98*, 134433. [CrossRef]
11. Egoavil, R.; Hühn, S.; Jungbauer, M.; Gauquelin, N.; Béché, A.; Van Tendeloo, G.; Verbeeck, J.; Moshnyaga, V. Phase problem in the B-site ordering of La_2CoMnO_6: Impact on structure and magnetism. *Nanoscale* **2015**, *7*, 9835–9843. [CrossRef]
12. Kleibeuker, J.E.; Choi, E.-M.; Jones, E.D.; Yu, T.-M.; Sala, B.; MacLaren, B.A.; Kepaptsoglou, D.; Hernandez-Maldonado, D.; Ramasse, Q.M.; Jones, L.; et al. Route to achieving perfect B-site ordering in double perovskite thin films. *NPG Asia Mater.* **2017**, *9*, e406. [CrossRef]
13. Barón-González, A.J.; Frontera, C.; García-Muñoz, J.L.; Rivas-Murias, B.; Blasco, J. Effect of cation disorder on structural, magnetic and dielectric properties of La_2MnCoO_6 double perovskite. *J. Phys. Condens. Matter* **2011**, *23*, 496003. [CrossRef] [PubMed]
14. Iliev, M.; Abrashev, M.V.; Litvinchuk, A.P.; Hadjiev, V.; Guo, H.; Gupta, A. Raman spectroscopy of ordered double perovskite La_2CoMnO_6 thin films. *Phys. Rev. B* **2007**, *75*, 104118. [CrossRef]
15. Kumar, D.; Sathe, V. Raman spectroscopic study of structural transformation in ordered double perovskites La_2CoMnO_6 bulk and epitaxial film. *Solid State Commun.* **2015**, *224*, 10–14. [CrossRef]
16. Kumar, D.; Kumar, S.; Sathe, V.G. Spin–phonon coupling in ordered double perovskites A_2CoMnO_6 (A = La, Pr, Nd) probed by micro-Raman spectroscopy. *Solid State Commun.* **2014**, *194*, 59–64. [CrossRef]
17. Filho, R.B.M.; Barbosa, D.A.B.; Reichlova, H.; Marti, X.; de Menezes, A.S.; Ayala, A.P.; Paschol, C.W.A. Role of ra-re-earth ionic radii on the spin–phonon coupling in multiferroic ordered double perovskites. *Mater. Res. Express* **2015**, *2*, 075201. [CrossRef]
18. Meyer, C.; Hühn, S.; Jungbauer, M.; Merten, S.; Damaschke, S.; Samwer, K.; Moshnyaga, V. Tip-enhanced Raman spectros-copy (TERS) on double perovskite La_2CoMnO_6 thin films: Field enhancement and depolarization effects. *J. Raman Spectrosc.* **2017**, *48*, 46–52. [CrossRef]
19. Xie, C.; Shi, L.; Zhao, J.; Zhou, S.; Li, Y.; Yuan, X. Spin-phonon coupling in R_2CoMnO_6 (R = Pr, Nd, Sm) thin films under biax-ial compressive strain. *J. Appl. Phys.* **2016**, *120*, 155302. [CrossRef]
20. Truong, K.D.; Singh, M.P.; Jandl, S.; Fournier, P. Influence of Ni/Mn cation order on the spin-phonon coupling in multifunc-tional La_2NiMnO_6 epitaxial films by polarized Raman spectroscopy. *Phys. Rev. B* **2009**, *80*, 134424. [CrossRef]
21. Truong, K.D.; Laverdière, J.; Singh, M.P.; Jandl, S.; Fournier, P. Impact of Co/Mn cation ordering on phonon anomalies in La_2CoMnO_6 double perovskites: Raman spectroscopy. *Phys. Rev. B* **2007**, *76*, 132413. [CrossRef]
22. Kumar, D.; Kumar, S.; Sathe, V.G. Raman studies of ordered double perovskite thin film at high temperatures. *NANOFORUM 2014* **2015**, 140030. [CrossRef]

23. Jungbauer, M.; Hühn, S.; Egoavil, R.; Tan, H.; Verbeeck, J.; Van Tendeloo, G.; Moshnyaga, V. Atomic layer epitaxy of Rud-dlesden-popper $SrO(SrTiO_3)_n$ films by means of metalorganic aerosol deposition. *Appl. Phys. Lett.* **2014**, *104*, 251603. [CrossRef]
24. Moshnyaga, V.; Belenchuk, A.; Hühn, S.; Kalkert, C.; Jungbauer, M.; Lebedev, O.I.; Merten, S.; Choi, K.-Y.; Lemmens, P.; Damaschke, B.; et al. Intrinsic antiferromagnetic coupling underlies colossal magnetoresistance effect: Role of corre-lated polarons. *Phys. Rev. B* **2014**, *89*, 024420. [CrossRef]
25. Norton, D.P. Synthesis and properties of epitaxial electronic oxide thin-film materials. *Mater. Sci. Eng. R Rep.* **2004**, *43*, 139–247. [CrossRef]
26. Shannon, R.D. Revised effective ionic radii and systematic studies of interatomic distances in halides and chalcogenides. *Acta Crystallogr.* **1976**, *32*, 751–767. [CrossRef]
27. Zhao, H.J.; Liu, X.Q.; Chen, X.M.; Bellaiche, L. Effects of chemical and hydrostatic pressures on structural, magnetic, and electronic properties of R_2NiMnO_6 (R = rare−earthion)double perovskites. *Phys. Rev. B* **2014**, *90*, 195147. [CrossRef]
28. Chen, Y.; Peng, A.B.; Wang, B. Raman Spectra and Temperature-Dependent Raman Scattering of Silicon Nanowires. *J. Phys. Chem. C* **2007**, *111*, 5855–5858. [CrossRef]
29. Granado, E.; García, A.; Sanjurjo, J.A.; Rettori, C.; Torriani, I.; Prado, F.; Sánchez, R.D.; Caneiro, A.; Oseroff, S.B. Magnetic ordering effects in the Raman spectra of $La_{1-x}Mn_{1-x}O_3$. *Phys. Rev. B* **1999**, *60*, 11879–11882. [CrossRef]
30. Laverdière, J.; Jandl, S.; Mukhin, A.A.; Ivanonv, V.Y.; Ivanov, V.G.; Iliev, M.N. Spin-phonon coupling in orthorhombic $RMnO_3$ (R = Pr, Nd, Sm, Eu, Gd, Tb, Dy, Ho, Y): A Raman study. *Phys. Rev. B* **2006**, *73*, 214301. [CrossRef]
31. Pandey, P.K.; Choudhary, R.J.; Mishra, D.K.; Sathe, V.G.; Phase, D.M. Signature of spin-phonon coupling in Sr_2CoO_4 thin film: A Raman spectroscopic study. *Appl. Phys. Lett.* **2013**, *102*, 142401. [CrossRef]
32. Jin, X.-W.; Lu, L.; Mi, S.-B.; Liu, M.; Jia, C.-L. Phase stability and B-site ordering in La_2NiMnO_6 thin films. *Appl. Phys. Lett.* **2016**, *109*, 31904. [CrossRef]
33. Balkanski, M.; Wallis, R.F.; Haro, E. Anharmonic effects in light scattering due to optical phonons in silicon. *Phys. Rev. B* **1983**, *28*, 1928–1934. [CrossRef]